Fluorine-labeled Dasatinib Nanoformulations as Targeted Molecular Imaging Probes in a PDGFB-driven Murine Glioblastoma Model[1,2]

Miriam Benezra*, Dolores Hambardzumyan[†,3], Oula Penate-Medina[*,3,4], Darren R. Veach*, Nagavarakishore Pillarsetty*, Peter Smith-Jones[‡], Evan Phillips*, Tatsuya Ozawa[§], Pat B. Zanzonico[¶], Valerie Longo*, Eric C. Holland[§,#,**], Steven M. Larson* and Michelle S. Bradbury[*,#]

*Department of Radiology, Sloan Kettering Institute for Cancer Research, New York, NY; [†]Department of Stem Cell Biology and Regenerative Medicine, Lerner Research Institute, Cleveland Clinic, Cleveland, OH; [‡]Department of Radiology, University of Colorado, Denver, Aurora, CO; [§]Department of Cancer Biology and Genetics, Sloan Kettering Institute for Cancer Research, New York, NY; [¶]Department of Medical Physics, Sloan Kettering Institute for Cancer Research, New York, NY; [#]Brain Tumor Center, Sloan Kettering Institute for Cancer Research, New York, NY; [**]Departments of Neurosurgery, Neurology and Surgery, Sloan Kettering Institute for Cancer Research, New York, NY

Abstract

Dasatinib, a new-generation Src and platelet-derived growth factor receptor (PDGFR) inhibitor, is currently under evaluation in high-grade glioma clinical trials. To achieve optimum physicochemical and/or biologic properties, alternative drug delivery vehicles may be needed. We used a novel fluorinated dasatinib derivative (F-SKI249380), in combination with nanocarrier vehicles and metabolic imaging tools (microPET) to evaluate drug delivery and uptake in a platelet-derived growth factor B (PDGFB)–driven genetically engineered mouse model (GEMM) of high-grade glioma. We assessed dasatinib survival benefit on the basis of measured tumor volumes. Using brain tumor cells derived from PDGFB-driven gliomas, dose-dependent uptake and time-dependent inhibitory effects of F-SKI249380 on biologic activity were investigated and compared with the parent drug. PDGFR receptor status and tumor-specific targeting were non-invasively evaluated in vivo using ^{18}F-SKI249380 and ^{18}F-SKI249380–containing micellar and liposomal nanoformulations. A statistically significant survival benefit was found using dasatinib (95 mg/kg) versus saline vehicle (P < .001) in tumor volume–matched GEMM pairs. Competitive binding and treatment assays revealed comparable biologic properties for F-SKI249380 and the parent drug. In vivo,

Significantly higher tumor uptake was observed for ^{18}F-SKI249380–containing micelle formulations [4.9 percentage of the injected dose per gram tissue (%ID/g); $P = .002$] compared to control values (1.6%ID/g). Saturation studies using excess cold dasatinib showed marked reduction of tumor uptake values to levels in normal brain (1.5%ID/g), consistent with *in vivo* binding specificity. Using ^{18}F-SKI249380–containing micelles as radiotracers to estimate therapeutic dosing requirements, we calculated intratumoral drug concentrations (24–60 nM) that were comparable to *in vitro* 50% inhibitory concentration values. ^{18}F-SKI249380 is a PDGFR-selective tracer, which demonstrates improved delivery to PDGFB-driven high-grade gliomas and facilitates treatment planning when coupled with nanoformulations and quantitative PET imaging approaches.

Neoplasia (2012) 14, 1132–1143

Introduction

Glioblastoma multiforme (GBM), the most common primary central nervous system tumor, requires aggressive local therapy and adjuvant chemotherapy to target widespread microscopic disease infiltration. These treatment combinations, however, confer only short-term survival benefit, and alternative therapeutic strategies have been increasingly incorporated into treatment planning protocols [1]. Mutations and activation of oncogenes contribute to GBM pathogenesis [2–5], leading to increased expression of receptor tyrosine kinases (RTKs). In addition, platelet-derived growth factor receptor (PDGFR) and non-receptor membrane-associated tyrosine kinases [i.e., Src family kinases (SFKs)] serve as attractive candidates for targeted tumor imaging and therapeutic intervention [6]. Inhibition of PDGFR leads to growth arrest and reduced tumor invasiveness, effects mediated through SFK activation [6–8]. Modest responses in high-grade glioma clinical trials using first-generation single-targeted kinase inhibitors have implicated several limitations relating to drug delivery, transporters, and compensatory kinase pathways [9,10].

Dasatinib (BMS354825, 488 g/mol), a highly potent second-generation ATP-competitive inhibitor of multiple protein tyrosine kinases [11–15], including PDGFR and SFKs [15,16], reduces tumor cell survival and proliferative and metastatic activity *in vitro*. In human GBM [17,18], PDGFRα, Src, and other known dasatinib targets are frequently activated. In this setting, dasatinib is currently being assessed in ongoing clinical trials of newly diagnosed and recurrent GBM [1].

The investigation of such novel agents for treating central nervous system tumors needs to consider issues relating to solubility, barrier penetration, drug uptake, and intratumoral distribution. These properties are not generally evaluated in the context of drug delivery due to the complexity of biologic systems and an inability to serially monitor this process non-invasively in the absence of drug labeling. One approach to accurately assess the above tumor-specific properties is to combine quantitative molecular imaging tools [i.e., micro–positron emission tomography (microPET)], with tracer doses of radiolabeled molecular probes or nanocarriers. This approach permits key physiologic and tumor-specific parameters to be defined, thus allowing pharmacologic doses to be estimated for image-guided targeted drug delivery and therapy [19].

In the present study, we examined the survival benefit of dasatinib, for the first time, in a clinically relevant platelet-derived growth factor B (PDGFB)–driven genetically engineered mouse model of high-grade glioma [i.e., murine glioblastoma multiforme (mGBM)] [20,21] to confirm previously established cellular profiles of target inhibition (i.e., PDGFRα, Src) [15]. Following synthesis of a newly modified fluorinated dasatinib derivative (F-SKI249380), and before *in vivo* imaging studies, we sought to determine the biologic equivalence of F-SKI249380 relative to the parent drug in terms of cell binding kinetics, dose-response behavior, cell cycle effects, PDGFR signaling, and inhibitory responses in tumor-derived primary glioma cell cultures. Incorporation of F-SKI249380 into micellar and liposomal nanocarriers was then performed to investigate whether improved drug delivery and uptake [percentage of the injected dose per gram tissue (%ID/g)] could be achieved in relation to the native fluorinated drug in PDGFB-driven mGBM.

Nanocarrier-encapsulated tracer preparations, along with microPET imaging, were used to develop a rational, translatable approach for estimating future *in vivo* therapeutic dosing requirements. We highlight the distinct advantages of using dynamic microPET imaging methods in combination with these tracer preparations to monitor the drug delivery process, localize the tumor, and extract the following key properties for individualizing treatment planning protocols: kinetics of tracer uptake and cumulative tracer concentrations.

Materials and Methods

Reagents, Antibodies, and Chemicals

Dulbecco's modified Eagle's medium–high glucose (DMEM-HG) media with 1.5 g/l sodium bicarbonate, fetal calf serum (FCS), penicillin, streptomycin, and Hank's balanced salt solution (HBSS; without calcium and magnesium containing 0.25% trypsin and 0.05% EDTA) were obtained from the Core Media Preparation Facility [Memorial Sloan-Kettering Cancer Center (MSKCC), New York, NY]. Anti-polyclonal rabbit, phospho-Erk1/2 (p-Erk1/2$^{Thr202/Tyr204}$), phospho-Akt (p-Akt^{Ser473}), phospho-Src (p-Src^{Tyr419}), phospho-p70S6 (p-p70S6^{Thr389}), phospho-MEK1/2 (p-MEK1/2$^{Ser217/221}$), Erk, Akt, Src, p70S6, and MEK1/2 (47E6) were obtained from Cell Signaling Technology (Danvers, MA). Goat anti-rabbit IgG, goat anti-mouse IgG HRP conjugates, and normal rabbit IgG were procured from Santa Cruz Biotechnology (Santa Cruz, CA). Anti–fluorescein isothiocyanate–Annexin V and 10× Annexin V binding buffer were obtained from BD Biosciences Pharmingen (San Jose, CA). Propidium iodide, DNase, RNase A, and recombinant human PDGFB were obtained from Invitrogen (Carlsbad, CA). Monoclonal anti–β-actin (clone AC-15) was supplied by Sigma-Aldrich (St Louis, MO). Ovomucoid and papain were procured from Worthington Biochemical Corporation (Lakewood, NJ). Dasatinib was obtained from US Biological (Swampscott, MA), and fluorinated dasatinib derivatives ([19]F-, ^{18}F-SKI249380) were synthesized

in-house. Both dasatinib and/or the fluorinated dasatinib derivative were used as competitors in these studies.

Synthesis of Chlorodasatinib (N-(2-chloro-6-methylphenyl)-2-(6-(4-(2-chloroethyl) piperazin-1-yl)-2-methylpyrimidin-4-ylamino)thiazole-5-carboxamide)

The chlorodasatinib precursor was prepared by chlorinating the free base of dasatinib (BMS354825) with mesyl chloride and triethylamine. BMS354825 (21 mg, 0.043 mmol), triethylamine (12 μl, 0.086 mmol), and 1 ml of anhydrous dimethylformamide (DMF) were added to a 5-ml screw-top vial under argon with magnetic stirring. The vial was cooled in an ice bath for 5 minutes. Methanesulfonyl chloride (5 μl, 0.065 mmol) was added, and the mixture was stirred for 15 minutes, allowed to warm to ambient temperature, and stirred for 12 hours. The reaction mixture was partitioned between 20 ml of CH_2Cl_2 and 20 ml of water. The organic layer was washed with water (2 × 10 ml) and brine (10 ml), dried over Na_2SO_4, filtered, and concentrated. The residue was resuspended in a small amount of CH_2Cl_2 and purification by gradient flash chromatography (SiO_2, 0% to 10% MeOH/CH_2Cl_2) yielded 12 mg (55%) of chlorodasatinib: ^1H NMR (DMSO-d_6), δ = 11.46 (s, 1H), 9.86 (s, 1H), 8.21 (s, 1H), 7.38 (dd, 1H, J = 7.6, 1.3 Hz), 7.29 to 7.22 (m, 2H), 6.04 (s, 1H), 3.71 (t, 2H, J = 6.7 Hz), 3.51 (br s, 4H), 2.68 (t, 2H, J = 6.6 Hz), 2.52 (br s, 4H), 2.40 (s, 3H), 2.23 (s, 3H); mass spectrometry-electrospray ionization (MS-ESI) theory, m/z = 506.13 $[M + H]^+$, found: 506.1; HPLC, t_R = 12.0 minutes [Phenomenex Gemini C18, 250 × 4.6 mm, gradient 70% A (20 mM KH_2PO_4, pH 4.1)/30% B (CH_3CN) to 20% A/80% B, 1 ml/min, λ = 254 nm].

Synthesis of ^{18}F-SKI249380

Cyclotron-produced $[^{18}F]$-HF in $[^{18}O]$-water was transferred to a solution containing 120 μl of 0.25 M K_2CO_3 (20 μmol) and 10 mg (2.7 μmol) of Kryptofix (2.2.2) in 0.5 ml of CH_3CN in a 10-ml Reacti-Vial. Water was removed azeotropically with CH_3CN (3 × 0.5 ml) at 105 to 110°C. Anhydrous $[^{18}F]$ KF/K_2CO_3, complexed with Kryptofix, was dissolved in 0.4 ml of CH_3CN, added to 3.0 mg (2.0 μmol) of chlorodasatinib, and heated (sealed) on a heating block (90°C, 45 minutes). The reaction mixture was cooled to room temperature and diluted with 1 ml of HPLC solvent (20% CH_3CN). The product was purified using HPLC [20%→80% CH_3CN in 50 mM NaOAc buffer (pH 5), 100 × 21.2 mm Gemini NX C18 column]. The product-containing fraction at t_R = 12.2 minutes was collected and concentrated to near dryness by rotary evaporation. The product was resuspended in 500 μl of saline and filtered through a 45-μm filter into a sterile vial. Total time of radiosynthesis was about 120 minutes from end of bombardment. Decay-corrected radiochemical yields were 18 ± 5% (n = 7) over two steps based on starting $[^{18}F]$-fluoride, and specific activity ranged from 300 to 600 mCi/μmol (n = 3). No significant contaminants were present in the final product.

Generation of a PDGFB-driven Glioma Cell Line

Primary mouse PDGFB-driven mGBM cell lines were generated from freshly isolated mGBM. Briefly, tumors were dissected and collected in 1× HBSS containing 0.6% glucose. Tissues were enzymatically digested in 1× HBSS containing 12% papain and 10 μg/ml DNase (37°C, 15 minutes) and subsequently inactivated with ovomucoid (1 mg/ml) as previously described [22]. Single-cell suspensions were prepared and cultured in DMEM-HG/1.5 g/l sodium bicarbonate medium supplemented with 10% FCS.

Generation of PDGFB-driven mGBM

All animal experiments were done in accordance with protocols approved by the Institutional Animal Care and Use Committee of MSKCC and followed National Institutes of Health guidelines for animal welfare. At 4 to 6 weeks of age, Nestin-tva/ink4a-arf$^{-/-}$ mice (n = 45) were injected intracranially with 4×10^4 DF-1 cells (ATCC, Manassas, VA) transfected with and producing Replication Competent ASLV long terminal repeat with Splice acceptor–PDGFB retroviral vector and using a stereotactic fixation device (Stoelting, Wood Dale, IL), as described previously [23]. Mice were monitored carefully for symptoms of tumor development (hydrocephalus, lethargy, and head tilt).

NIH 3T3 Fibroblasts Expressing PDGFRα-myc

Fibroblasts expressing the PDGFRα-myc receptor were generated by infecting NIH 3T3 cells with retroviral expression vectors encoding PDGFRα [18]. Cells were grown and maintained in DMEM-HG/1.5 g/l sodium bicarbonate medium supplemented with 10% calf serum (Colorado Serum Company, Denver, CO).

In Vitro *Receptor Binding Assays*

Competitive PDGFR binding studies and kinetic analyses were performed by co-incubating PDGFB-driven mGBM cells with ^{19}F-dasatinib (^{19}F-SKI249380) or dasatinib (BMS354825) and adding ^{18}F-dasatinib (^{18}F-SKI249380). Briefly, triplicate samples of ^{18}F-dasatinib (^{18}F-SKI249380; 20,000 cpm) and increasing amounts (0.001–1000 nM) of non-radiolabeled competitor were mixed with cells on an orbital shaker (1 hour, 25°C). Cells were then isolated by rapid filtration, washed with ice-cold TBS using a cell harvester (Brandel, Gaithersburg, MD), and counted, along with suitable blanks, using a γ-counter (Perkin Elmer 1480 Wizard 3, Waltham, MA). Nonspecific and specific uptake of ^{18}F-SKI249380 was determined, the former in the presence of 1000 nM ^{19}F-SKI249380. These data were plotted against the concentration of cold competitors, and sigmoidal displacement curves were analyzed by a least-squares fitting algorithm (Origin, Northampton, MA). Scatchard analysis of the saturation binding kinetic curve for SKI249380 yielded the equilibrium dissociation constant, K_d, and total number of available bound receptor sites per cell, B_{max}.

Cell Viability Assays with ^{19}F-SKI249380

mGBM cells, expressing PDGFB-encoding viruses, were seeded into 24-well culture plates. In one set of treatment studies, ^{19}F-SKI249380 was added to 6.0×10^4 cells/well in media supplemented with 10% FCS over a range of concentrations (2.5–500 nM) for 72 hours, whereas in a second set of studies, two concentrations (10 and 50 nM) were added to 2.5×10^4 cells/well every 48 hours over a range of incubation times (0–8 days). The percent (%) cell viability was determined after trypsinization using a Vi-Cell series viability analyzer (Beckman Coulter, Inc, Fullerton, CA). In a parallel set of experiments, mGBM cells were made quiescent under serum-deprived conditions (DMEM/1.5 g of sodium bicarbonate containing 0.2% FCS) at 37°C for 96 hours before treatment for G_0/G_1 phase synchronization. Cells then underwent a medium change to one containing 0.2% FCS (control media), 10% FCS, or 0.2% FCS supplemented with PDGF (25 ng/ml) and were subsequently incubated at 37°C with or without ^{19}F-SKI249380. Each experiment was performed in triplicate.

Cell Cycle Analysis

G_0/G_1 phase–synchronized mGBM cells were incubated for 72 hours using a range of ^{19}F-SKI249380 concentrations (0–1000 nM) after changing the medium to 10% FCS. Following trypsinization, cells were centrifuged (1200 rpm, 5 minutes), and the pellet was suspended in phosphate-buffered saline (PBS), followed by fixation with 70% ethanol (0.5–1 hour, 4°C). Cells were successively resuspended in 1 ml of PBS containing 1% FCS and 0.1% Triton X-100, 200 μl of PBS containing 25 μg/ml propidium iodide, and 100 μg/ml RNase A (4°C, 60 minutes). Cell cycle analysis was performed by flow cytometry (FACSCalibur; Becton Dickinson, Mountain View, CA) and Phoenix Flow MultiCycle software (Phoenix Flow Systems, Inc, San Diego, CA).

Apoptosis and Necrosis

mGBM cells, initially grown under serum-deprived conditions, were subsequently incubated with ^{19}F-SKI249380 (0–1000 nM) for 72 hours in 10% FCS–supplemented media. After trypsinization, cells were centrifuged (1200 rpm, 5 minutes) and resuspended in 200 μl of 1× Annexin V binding buffer. The solubilized pellet (100 μl) was incubated in the dark (25°C, 15 minutes) with 5 μl of fluorescein isothiocyanate–Annexin V and 2.5 μl of propidium iodide (50 mg/ml), followed by addition of 100 μl of 1× Annexin V binding buffer for determination of the apoptotic cell fraction (%) using flow cytometry and FloJo analysis software (v. 8.8; Tree Star, Ashland, OR).

Western Blot

As above, mGBM cells were made quiescent and grown under serum-deprived conditions. The medium was then changed to 10% FCS or 0.2% FCS supplemented with 25 ng/ml PDGF, and 150 nM ^{19}F-SKI249380 was added over a range of time intervals (5–60 minutes). Cells were rinsed twice in ice-cold PBS and collected by trypsinization, and the pellet was resuspended in lysis buffer [10 mM Tris (pH 8.5), 150 mM NaCl, 1 mM EDTA, 1% Triton X-100; ACROS Organics, Fair Lawn, NJ], 1% sodium deoxycholate, 0.1% sodium dodecyl sulfate (SDS), Complete protease inhibitors (Roche, Indianapolis, IN), and phosphatase inhibitor cocktails 1 and 2 (Sigma-Aldrich). Lysates were centrifuged (10 minutes, 4°C). Protein concentrations were determined by the bicinchoninic acid assay (Thermo Scientific, Rockford, IL). A protein aliquot (30–50 μg) of each fraction was separated by 4% to 12% gradient SDS–polyacrylamide gel electrophoresis and transferred to a polyvinylidene fluoride (PVDF) membrane (Invitrogen). Membranes were blocked with 5% non-fat dry milk (Bio-Rad, Hercules, CA) in TBS–0.1%Tween and signal visualized by enhanced chemiluminescence (Thermo Scientific) after applying primary (1:1000) and secondary (1:2000–1:5000) antibodies.

Immunoprecipitation

mGBM cells were grown under serum-deprived conditions. The medium was then changed to 10% FCS or 0.2% FCS with 25 ng/ml PDGF, and 250 nM ^{19}F-SKI249380 was added for 10 minutes. After cells were lysed in 1% NP-40 lysis buffer [50 mM Tris (pH 8.0), 50 mM NaCl, 5 mM EDTA, 1% NP-40, protease inhibitors, and phosphatase inhibitors], lysates were incubated (2 hours, 4°C) with anti–c-myc agarose Affinity gel (Sigma-Aldrich), followed by multiple washings with the same buffer. Immunoprecipitated proteins were resolved by 5% SDS–polyacrylamide gel electrophoresis and analyzed by Western blot (WB) analysis with phosphotyrosine (Cell Signaling Technology), c-myc (clone-9E10; Sigma-Aldrich), and PDGFRα (Cell Signaling Technology) antibodies using enhanced chemiluminescence for visualization.

Survival Studies

Three weeks after intracranial inoculation, gradient echo images of brain tumors ($n = 16$) were acquired in the coronal plane on a 4.7-Tesla magnetic resonance imaging (MRI) scanner (Bruker Biospin, Billerica, MA) using a birdcage coil and the following MRI parameters: TR = 2500 ms, TE = 50 ms, field of view = 3 × 2 cm, slice thickness (with interslice distance = 0.7 mm) = 0.7 mm, matrix = 256 × 128, NEX = 28. Mice were anesthetized using 2% isoflurane anesthesia in oxygen during the scan period. Three-dimensional region-of-interest (3D-ROI) analyses (Paravision 4.0 software; Bruker) of brain tumor mice were performed to assess tumor volumes; volume-matched pairs of mice were assigned to either treatment or control groups for survival studies. Tumor volumes (mm^3) were computed on sequential MRI slices by summing the products of the slice areas and slice thicknesses over the full extent of the tumor. Mice were orally gavaged with dasatinib (95 mg/kg) or saline vehicle (200 μl) for 10 consecutive days, and daily weights were recorded. At treatment termination, all mice underwent repeat MRI to assess changes in tumor volumes. Tumor volume ratios were computed by dividing post-treatment (day 10) by pre-treatment (day 0) values for individual mice and as cohort averages. All mice were monitored daily, during, and following treatment and sacrificed for lethargy, hunched appearance, respiratory distress, >15% body weight loss, or neurologic impairment.

Micellar Formulated ^{18}F-SKI249380

Monomers or polyethylene glycol (PEG) 3400–distearoylphospha-tidylethanolamine (DSPE) spontaneously formed micelles on the order of 10 nm in diameter in the absence of drug loading, with DSPE lipid chains comprising the hydrophobic core and PEG chains coating the hydrophilic surface of the micelle. After ^{18}F-SKI249380 loading of micelles, their average size increased to 50 nm in diameter. ^{18}F-SKI249380 was hydrated with 0.9% NaCl and PEG3400-DSPE (30 minutes at 60°C).

Liposomal Formulated ^{18}F-SKI249380

Lipid stock solutions were prepared in chloroform to obtain the desired composition. Solvent was removed under a gentle stream of nitrogen, and the lipid residue was maintained under reduced pressure for at least 2 hours. Multilamellar liposomes (PC/Chol, 70/30 mol/mol) were formed by hydrating dry lipids at room temperature with 1 ml of PBS containing 1 to 2 mCi ^{18}F-SKI249380, facilitating its encapsulation into liposomes, and yielding a lipid concentration of 20 mM. Large unilaminar vesicles were obtained by extruding multilamellar dispersions 19 times through a 100-nm pore-size polycarbonate membrane (Nucleapore, Pleasanton, CA) with a Mini Extruder (Avanti Polar Lipids, Alabaster, Alabama).

Characterization of Nanocarriers

Size measurements were obtained using dynamic light scattering (DLS, Malvern Nano-S; Malvern Instruments, Worcestershire, United Kingdom). Measurements were based on differences in light backscattering properties of different size particles. To evaluate the critical micellar concentration (CMC), we sized micelles over a range of concentrations [24]. The radiolabeled dasatinib-loading densities of micelles and liposomes were calculated using the specific activities of ^{18}F-SKI249380, the overall activity of dasatinib nanocarriers (kcps), and the total amount of lipid.

MicroPET Imaging

Imaging was performed on a dedicated small-animal PET scanner (Focus 120 microPET; Concorde Microsystems, Knoxville, TN). PDGFB-driven mGBM mice ($n = 20$) were maintained under 2% iso-flurane anesthesia in oxygen during the scan. One-hour list-mode acquisitions were initiated at the time of intravenous (i.v.) injection of 1.1 to 1.5×10^7 Bq of the fluorinated dasatinib derivative, ^{18}F-SKI249380 ($n = 3$), or ^{18}F-labeled dasatinib nanocarriers in tumor-bearing mice ($n = 5$ mice each for micelles and liposomes). In addition, ^{18}F-SKI249380 was injected i.v. into non–tumor-bearing age-matched controls ($n = 4$). Voxel count rates in reconstructed images were con-verted to activity concentrations (i.e., %ID/g) using a measured system calibration factor. 3D-ROI analyses of reconstructed images (ASIPro software; Concorde Microsystems) yielded mean, maximum, and SD of tumor uptake.

In Vivo PDGFR Blocking Studies

Thirty minutes after i.v. injection of a single pharmacologic dose of non-radiolabeled dasatinib (~5 μM, 200 μl), tracer doses of ^{18}F-SKI249380 were administered i.v. ($n = 3$), followed by 1-hour list-mode PET acquisitions. Average "post-block" tumor activity–concentration values were determined and compared with correspond-ing "pre-block" values derived 3 days earlier in the same animals.

Biodistribution Studies

mGBM mice ($n = 9$ mice; three mice per time point) were i.v. injected with a micellar nanoformulation of ^{18}F-SKI249380 (~100 μCi/mouse) before 30-minute list-mode PET acquisitions at 15 minutes, 1 hour, and 4 hours post-injection (p.i.). *Ex vivo* %ID/g values, corrected for radioactive decay to the time of injection, were measured by sacrificing mice at 4 hours p.i. and harvesting, weighing, and counting blood, tumor-bearing brain, and organs in a scintilla-tion γ-counter. The small brain size of the mice and the diffuse, infiltrative nature of these tumors limited differentiation of tumors from the normal brain in the same animal. Image-derived %ID/g values of tumor-bearing brain, liver, heart, and muscle were addition-ally determined at each time point by performing 3D-ROI analyses; measurements at 4 hours were correlated with *ex vivo* values.

Statistics

Competitive binding assays and corresponding Scatchard plots were analyzed by linear regression analyses (Microsoft Excel 2007) to de-rive receptor binding parameters [K_d, B_{max}, and 50% inhibitory con-centration (IC$_{50}$)]. Goodness-of-fit values (R^2) and their associated P values are indicated. The Mann-Whitney U test was used to test statistical significance of tumor volume ratios and imaging data, expressed as the mean tumor uptake value (%ID/g) ± SD. We assigned statistical significance for all tests at $P < .05$. Correlation of image- and γ-counter–derived %ID/g values was performed using a least-squares regression algorithm (SigmaPlot, Systat, v. 11.0). The Kaplan-Meier method and log-rank test were used to evaluate survival curves. Survival of each mouse was recorded as the length of time from treatment initiation to demise.

Results

Competitive PDGFRα Receptor Binding of Dasatinib and ^{19}F-SKI249380 to mGBM Cells

The radiotracer, ^{18}F-SKI249380, previously prepared by a two-step procedure [15], was synthesized as a newly modified one-step approach using the chlorinated analog of dasatinib (Figure 1). The binding spec-ificity of ^{18}F-SKI249380 to mGBM cells was investigated in the pres-ence of non-radiolabeled competitors, ^{19}F-SKI249380 and dasatinib. Displacement curves were found to be equivalent over a range of con-centrations (Figure 2A). The IC$_{50}$ values were similar at 10.5 ± 2.8 nM for ^{19}F-SKI249380 and 13.6 ± 2.1 nM for dasatinib. The saturation binding data and Scatchard transformation (Figure 2B) of ^{18}F-SKI249380 binding to mGBM cells yielded a K_d of 6.3 ± 0.5 nM and a B_{max} of $1.2 \times 10^6 \pm 1.9 \times 10^4$ (Figure 2B, inset).

### Alterations in mGBM Cell Viability and Growth Rate with Dasatinib and ^{19}F-SKI249380

Cultured PDGFB-driven mGBM cells were monitored for reduc-tions in viability and growth rate following exposure to two doses of dasatinib or ^{19}F-SKI249380 over a range of concentrations and incu-bation times. Dose-response curves, 120 hours after seeding, revealed a concentration-dependent inhibition below about 150 nM. Net viabil-ity losses averaged about 80% using at least 50 nM concentrations of either agent. Beyond 150 nM, no such dependency was observed (Figure W1A). On the basis of these data, IC$_{50}$ values of 9 and 12 nM were computed for dasatinib and ^{19}F-SKI249380, respectively. In ad-dition, net growth inhibition was relatively constant for cells incu-bated with about 50 nM ^{19}F-SKI249380 or dasatinib (replaced every 48 hours) over an 8-day period (Figure W1B). Up to 85% inhibition was seen at 50 nM relative to that at 10 nM; at this latter concentra-tion, a net increase in cell number was noted over time. On the basis of equivalent dose-response and competitive binding data measured for dasatinib and ^{19}F-SKI249380, the fluorinated derivative was used for subsequent *in vitro* and *in vivo* testing.

mGBM Viability Loss with ^{19}F-SKI249380 in PDGFB-supplemented Media

Initial maintenance of cells under serum-deprived conditions en-abled G$_0$/G$_1$ synchronization of the majority of mGBM cells before assessing biologic response to different media conditions. Addition of 10% FCS to G$_0$/G$_1$ phase–synchronized cells led to a quadrupling of cell number relative to that for control media (Figure W1C), whereas 0.2% FCS supplemented with 25 ng/ml PDGFB ligand resulted in a doubling of cell number (Figure W1D), likely due to greater growth factor enrichment of serum-supplemented media. Progressive viability losses were observed following addition of increasing ^{19}F-SKI249380 concentrations to 10% FCS–supplemented cells; losses were greater in the presence of PDGF-supplemented media. After exposure to 150 nM ^{19}F-SKI249380, cell survival was reduced by factors of 2 and 6 for 10% FCS (Figure W1C)– and PDGF-supplemented (Fig-ure W1D) media, respectively.

Influence of ^{19}F-SKI249380 on Cell Cycle and Apoptosis of mGBM Cells

To analyze the effect of ^{19}F-SKI249380 on the cell cycle and apop-tosis, we incubated G$_0$/G$_1$ phase–synchronized mGBM cells for 72 hours over a range of ^{19}F-dasatinib concentrations (0–1000 nM) in 10% FCS–supplemented media. Over this range, the percentage of cells in the G$_1$ phase rose by 31%, whereas a corresponding 67% decline was seen in the proliferative or S phase of the cell cycle. A smaller drop (~40%) was noted in the G$_2$ phase (Figure W2A). No significant change in the percentage of cells in the G$_1$ or S phase was seen for ^{19}F-SKI249380 concentrations of 200 nM or higher. The
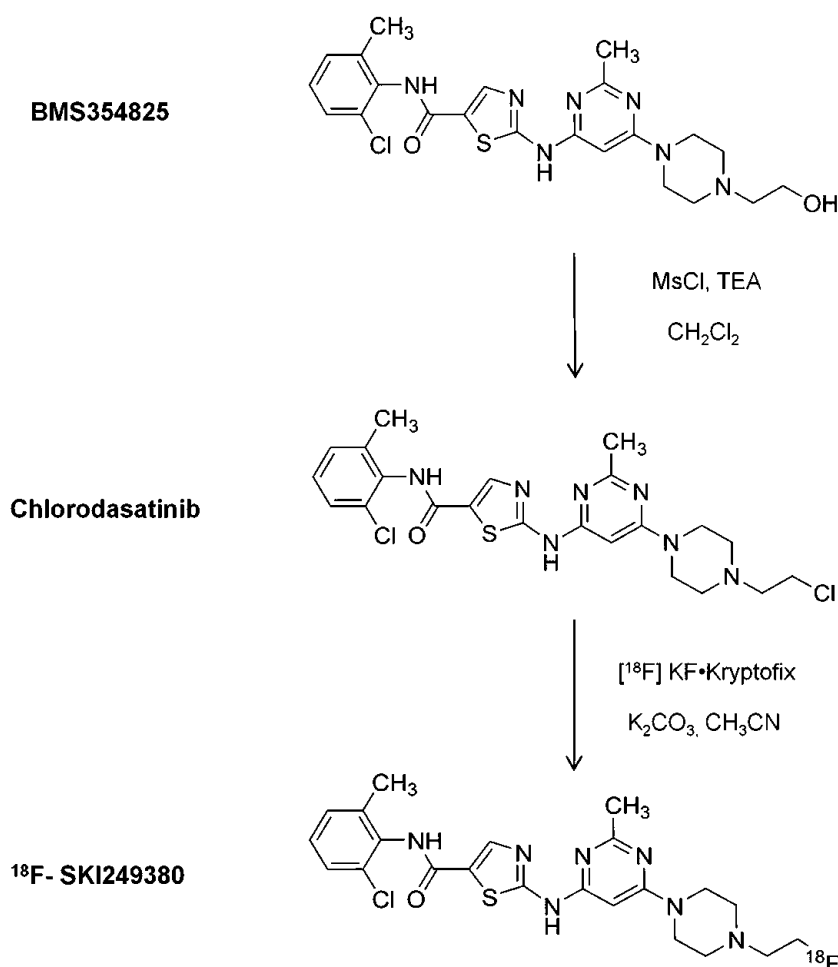
Figure 1. Schematic of the synthesis of ^{18}F-SKI249380 from dasatinib. BMS354825 is chlorinated with mesyl chloride and triethylamine. The resulting chlorodasatinib precursor is radiofluorinated using no carrier–added [^{18}F]KF·Kryptofix [2.2.2] complex.

fraction of cells undergoing apoptotic cell death before and after exposure to a range of ^{19}F-SKI249380 concentrations is seen to increase by more than a factor of 2 for order of magnitude changes in concentration, as shown in Figure W2B along with scatter plots at three representative concentrations. Further, cleaved poly (ADP-ribose) polymerase (PARP) protein was expressed on WBs for ^{19}F-SKI249380 concentrations of 250 nM and higher (data not shown). Taken together, these data indicate G$_1$ arrest with significant inhibitory effects on cell proliferation, along with a smaller cellular apoptotic component.

Inhibitory Effects of Dasatinib on PDGFRα and PDGFR-mediated Signaling

The binding of the PDGFB ligand to its receptor and subsequent receptor autophosphorylation at tyrosine residues is known to rapidly activate multiple signaling cascades and downstream pathway intermediates (Figure 3A), including Ras–mitogen-activated protein signaling, which induces activation of Raf/MAPK/Erk kinase (MEK)/Erk and phosphatidylinositol 3-kinase/Akt pathways [Akt, mammalian target of rapamycin (mTOR), S6K] [25–27], as well as SFKs [28–30] (Figure 3A). To determine whether ^{19}F-SKI249380 inhibited activation of PDGFR-mediated signaling, we treated serum-deprived NIH 3T3 cells, expressing myc-tagged PDGFRα, with 250 nM ^{19}F-SKI249380 in the presence of 10% FCS or 0.2% FCS supplemented with PDGF

ligand; non-treated and serum-deprived cells without PDGF served as controls. Immunoblot analysis of proteins, derived from the resulting immunoprecipitated lysates and analyzed by WB using phosphotyrosine, c-myc, and PDGFRα antibodies, demonstrated phosphorylation of tyrosine residues on PDGFRα, induced by 10% FCS or 0.2% FCS with PDGF ligand (Figure 3B). This result was not seen in treated cells incubated with 10% FCS, 0.2% FCS supplemented with PDGF ligand, or serum-deprived cells. WBs of lysates immunoprecipitated with myc antibody revealed that the amounts of protein in the samples were equivalent and that PDGFRα expression was present in lysates incubated with anti-PDGFRα antibody (Figure 3B). Collectively, these results suggested that ^{19}F-SKI249380 inhibits phosphorylation of PDGFRα.

In mGBM cells, downstream signaling pathways were also altered by the inhibition of PDGFR phosphorylation with ^{19}F-SKI249380. WB analyses of untreated cell lysates revealed activation of pathway intermediates in cells supplemented with 10% FCS or PDGF ligand. Treatment with 150 nM ^{19}F-SKI249380 showed subsequent inhibition of expression levels over a range of incubation times (Figure 3C). In cells incubated with 0.2% FCS/PDGF ligand or 10% FCS, there was a marked reduction in the phosphorylation levels of phospho-Rous sarcoma oncogene homolog (pSrc), phospo-MAPK/Erk kinase (pMEK), phospho-extracellular signal-regulated kinase (pERK), and phospho-AKT8 virus oncogene cellular homolog (pAkt) within 5 minutes of ^{19}F-SKI249380 exposure; these levels did not vary substantially

among these different media conditions. A sustained reduction (up to 72 hours) in pSrc expression was observed (data not shown). By contrast, a decrease in S6K phosphorylation levels was not seen for about 30 minutes post-treatment.

Survival Benefit of Dasatinib in PDGFB-driven mGBM

MRIs were acquired before and after 10 consecutive days of orally gavaged saline vehicle or dasatinib treatment (Figure 4A). Daily weight measurements of mice revealed no significant weight fluctuation for the dasatinib-treated group over the treatment interval. Tumor volume ratios were computed for each mouse; mean values showed a statistically significant decrease in magnitude for dasatinib-treated mice *versus* controls ($P < .001$, Figure 4B). Tumor volume ratios of volume-matched mouse pairs show appreciable differences within each pair (Figure 4C). Pre-treatment tumor volumes are indicated above each column. Survival was monitored in all mice following the end of treatment. Mice gavaged with saline vehicle survived 14 to 17 days post-treatment (mean, 15.5 days), whereas dasatinib-gavaged mice survived 18 to 30 days (mean, 25.75 days; $P < .001$, Kaplan-Meier Survival analysis; Figure 4D).

Micelle- and Liposome-encapsulated ^{18}F-SKI249380 as Suitable Drug Delivery Vehicles

^{18}F-SKI249380 was loaded into PEGylated water-soluble nanocarriers, and the resulting platforms were characterized by DLS. Average diameters of micelle and liposome formulations of ^{18}F-SKI249380 were 50 and 120 nm, respectively (Figure W3A). The size distribution, as determined by DLS, is presented according to the percentage of backscattered intensity (Figure W3B). Fitted curves of micelle size distribution and activity are presented as a function of increasing PEG-phosphoethanolamine (PEG-PE) concentration (Figure 5A). The data derived from these curves, namely, the PEG-PE concentration at which micelle size no longer increases (slope = 0), as well as the value at which micelle activity initially increases (slope > 0), were used to estimate a CMC of PEG-PE dasatinib < 10 µM. The CMC is defined as the concentration of amphiphilic molecules above which micelles can form and incorporate drug molecules; below this level, micelles will degrade, and the drug will be rapidly released. In addition to nanocarrier size, loading densities of ^{18}F-SKI249380 [drug/lipid (mol/mol) ratio] were found to be 1/233 and 1/2000 (mol/mol) for micelles and liposomes, respectively (Figure 5B). Yields of encapsulated ^{18}F-SKI249380 are also shown.

Dynamic PET Imaging of ^{18}F-SKI249380 Nanoformulations

Differential uptake of unencapsulated ^{18}F-SKI249380, as well as of micellar and liposomal ^{18}F-SKI249380 formulations, was investigated in glioma- and non–glioma-bearing mice (controls) by microPET imaging. Representative coronal images from glioma-bearing mice administered non-encapsulated and nanoformulated ^{18}F-SKI249380 revealed uptake of the radiotracer in the majority of mice over a 1-hour time period; no appreciable uptake was observed in control mice
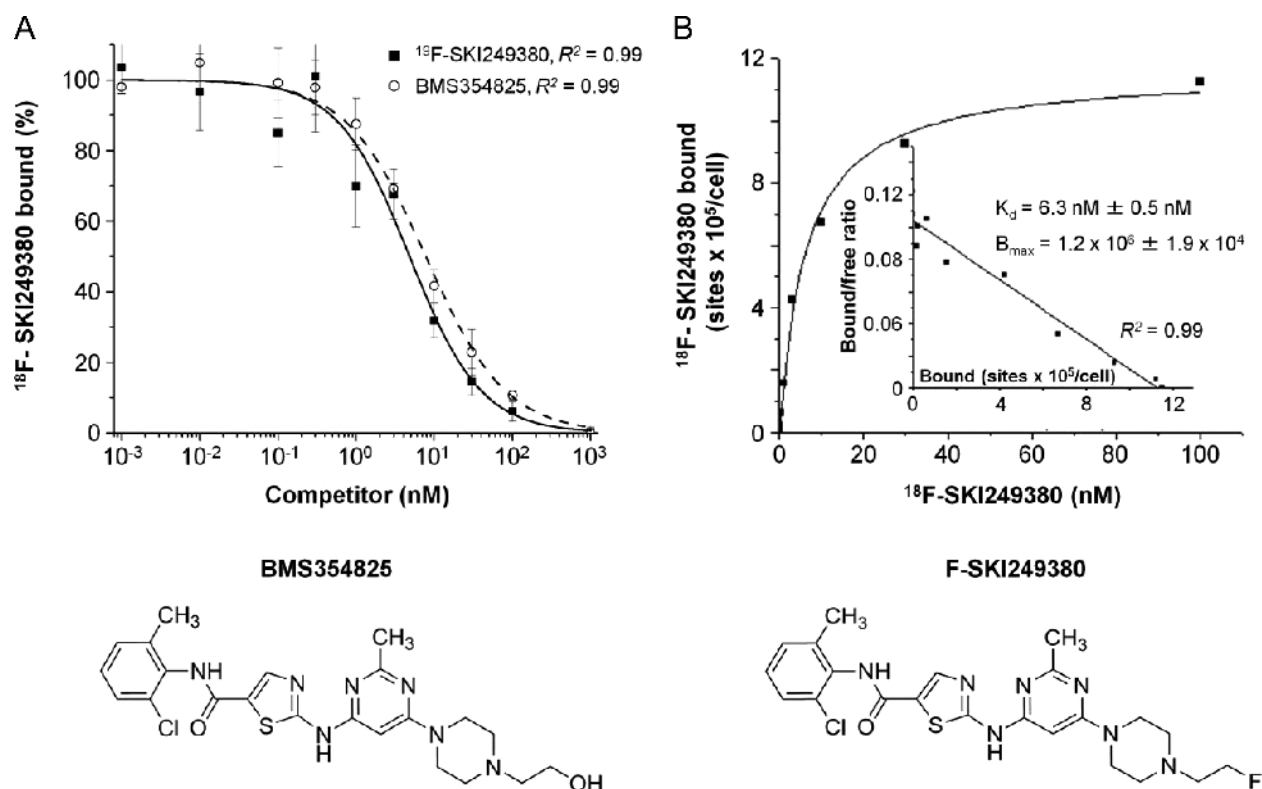
Figure 2. *In vitro* competitive PDGFRα receptor binding kinetics with ^{19}F-SKI249380, dasatinib, and ^{18}F-SKI249380 in mGBM cells using a range of concentrations (0.001–1000 nM). (A) High affinity and specific binding of ^{18}F-SKI249380 to mGBM cells after co-incubating with ^{19}F-SKI249380 or dasatinib and γ-counting. (B) Saturation binding kinetics of ^{18}F-SKI249380 to mGBM cells. The inset shows Scatchard analysis of binding data, plotting the ratio of the concentration of receptor-bound (B) to unbound (or free [F]) radioligand or the bound-to-free ratio (B/F) *versus* the receptor-bound receptor concentration; the slope corresponds to the K_d and x-intercept corresponds to receptor concentration. Schematics of BMS354825 (dasatinib) and the fluorinated dasatinib derivative, F-SKI249380, are shown.
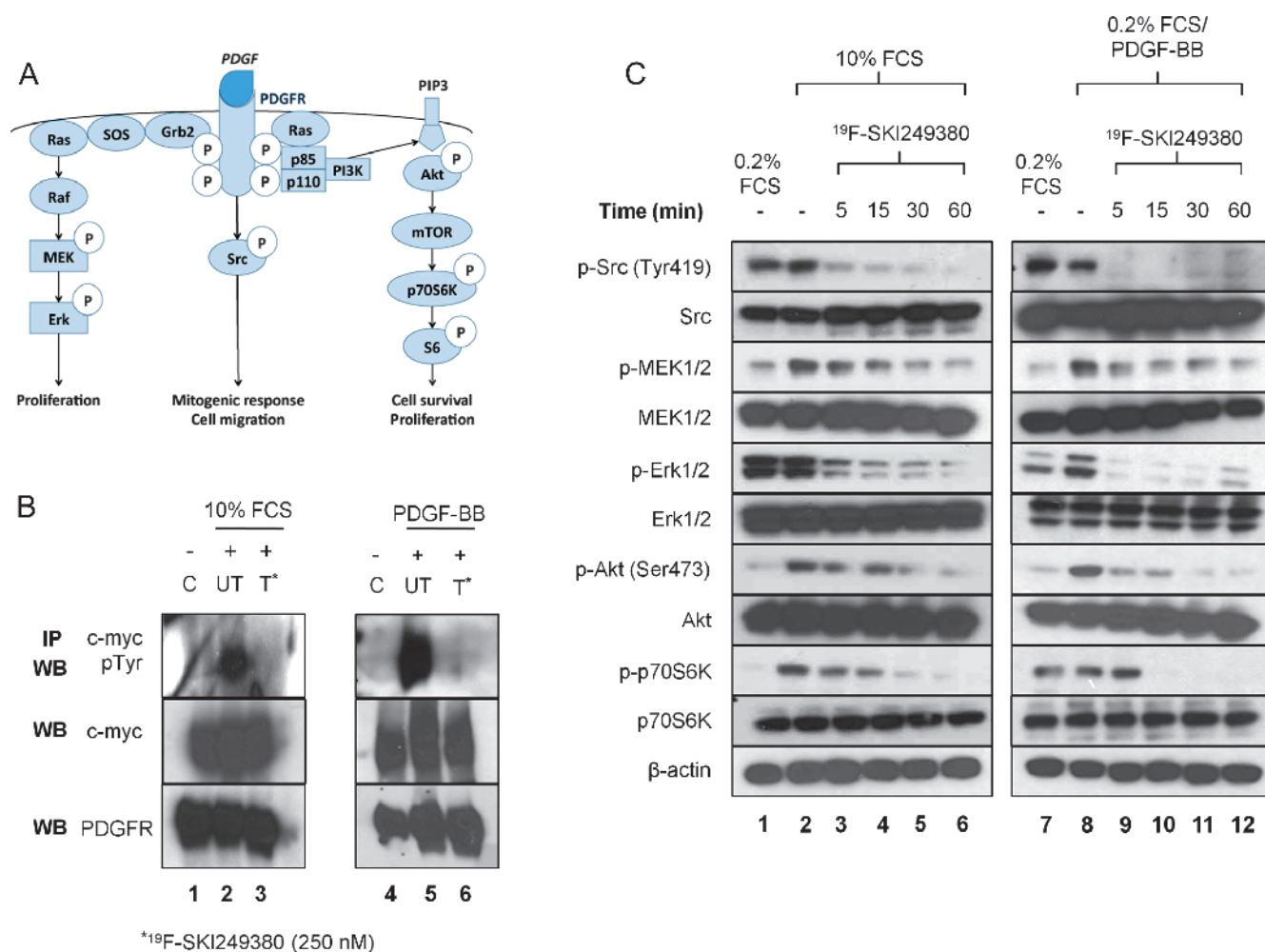
Figure 3. *In vitro* dasatinib treatment exhibits an inhibitory effect on PDGFR receptor activity and shows targeted inhibition of phosphorylated Src, MEK, Erk, Akt, and p70S6. (A) Schematic demonstrating multiple downstream PDGFR signal transduction pathways. (B) Lysates from NIH 3T3 cells expressing PDGFRα-myc were immunoprecipitated with myc antibody. WBs were probed for the presence of phosphotyrosine (upper panel), myc protein (middle panel), or PDGFRα (lower panel). Before treatment with 250 nM ^{19}F-SKI249380, cells were cultured in 0.2% FCS (lanes 1 and 4), 0.2% FCS/PDGF (lane 5), or 10% FCS (lane 2); after treatment in 10% FCS (lane 3) or 0.2% FCS/PDGF (lane 6). (C) Phosphorylation of Src, MEK, Erk, Akt, and p70S6 was assessed by WB for cells in 0.2% FCS, 10% FCS, or 0.2% FCS with/without PDGF and before and after the addition of 150 nM ^{19}F-SKI249380 for fixed incubation times. β-Actin was employed as a loading control. Representative of three independent experiments.

(Figure 6A). Injection of unencapsulated ^{18}F-SKI249380 resulted in an average tumor uptake of 3.4 ± 0.57%ID/g, as compared with 1.6 ± 0.39%ID/g in non–tumor-bearing brains. Micelle and liposome ^{18}F-SKI249380 formulations were prepared. No adverse reactions were observed following i.v. administration of these formulations. Average micelle and liposome ^{18}F-SKI249380 tumor uptake values of 4.9% ID/g ± 0.85 (P = .002) and 3.5%ID/g ± 0.57 (P = .014), respectively, were found to be significantly greater than that in the brains of control animals (Figure 6B). Differences between average micelle and liposome uptake (P = .016), as well as between average micelle and unencapsulated ^{18}F-SKI249380 uptake (P = .052), were also statistically significant. There was no significant difference between the average uptake values for liposomes and unencapsulated ^{18}F-SKI249380.

In vivo blocking studies were performed to evaluate receptor specificity. Single pharmacologic doses of non-radiolabeled dasatinib were injected 30 minutes before i.v. injection of ^{18}F-SKI249380 and dynamic PET. Significant suppression of tumor uptake values was observed for the post-block time-activity curve (TAC) compared to

baseline (pre-block) TAC values and was similar to that found for non–tumor-bearing mice. These findings suggested that receptor binding was fully saturated, preventing further ^{18}F-SKI249380 uptake (Figure 6C). The pre-block TAC in tumor-bearing mice showed a rise in %ID/g over time, reaching its previously reported value at about 30 minutes p.i.

On the basis of the specific activity of radiolabeled nanocarriers (i.e., $1.1–2.2 \times 10^{10}$ Bq/μmol) and the administered activity (i.e., $1.1–1.5 \times 10^{7}$ Bq), the total amount of injected ^{18}F-SKI249380 was found to range from 0.5 to 1.3 nmol. Together with the maximum tumor uptake for i.v.-injected micellar formulations (i.e., 4.9%ID/g at 1 hour), this yields intratumoral concentrations ranging from 24 to 64 pmol/g (or 24–60 nM). These concentrations are of the order of the ^{19}F-SKI249380 IC_{50} value of 11 nM, determined from competitive binding assays. That the minimum tumor concentration is comparable to the IC_{50} value for this delivery system suggests that, as an initial approximation, at least two doses of inhibitor may be needed to achieve significant tumor cell kill (i.e., reduce tumor cell survival to
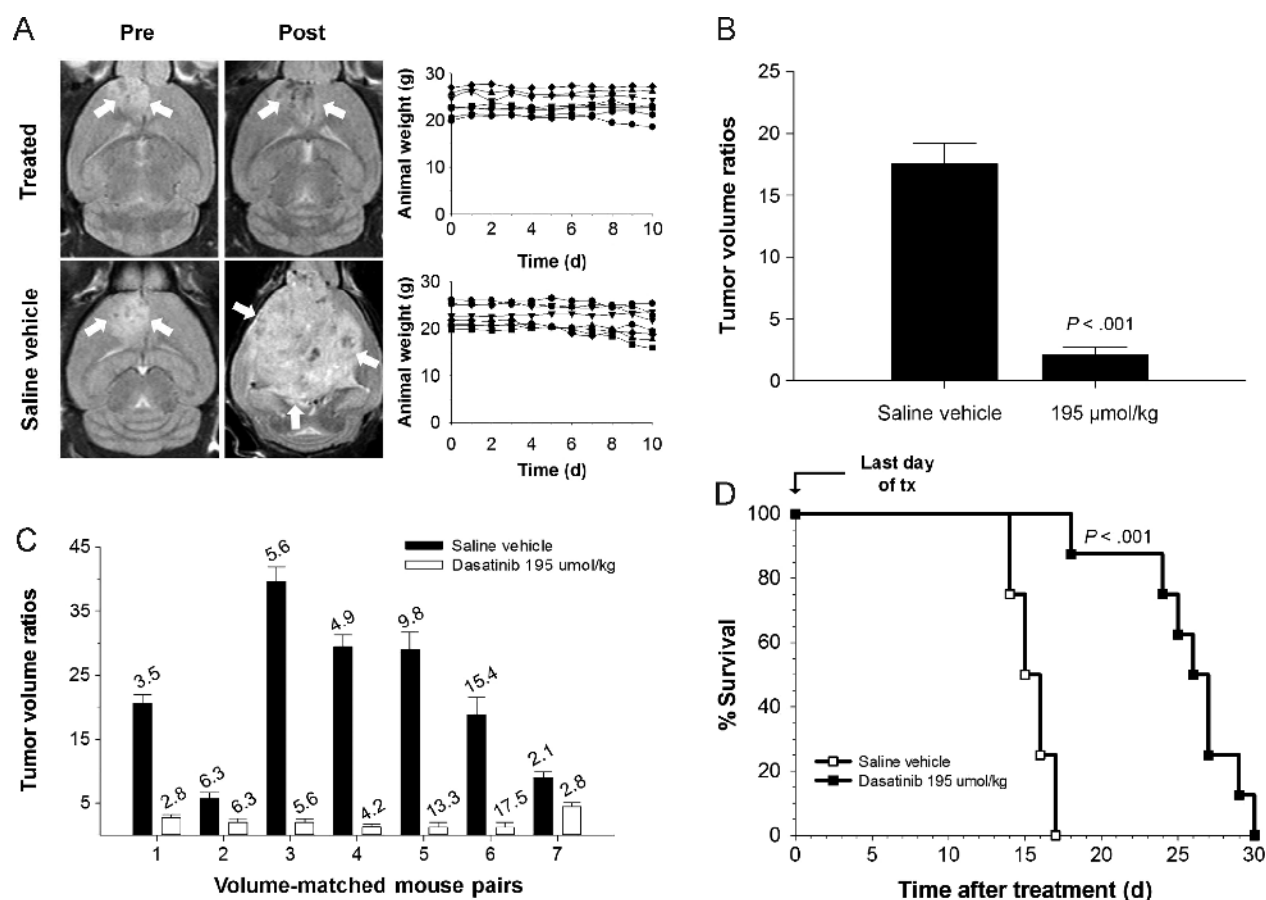
Figure 4. Volume-matched pairs of mice with PDGFB-driven mGBM show a survival benefit after gavage with dasatinib. (A) MRIs of brain tumors (white arrows) before and after administration of dasatinib or saline vehicle. (B) Graphical summary of average tumor volume ratios for treated and control groups (Mann-Whitney U test, $P < .001$). (C) Tumor volume ratios at 10 days post-treatment relative to pre-treatment values for individual pairs of volume-matched mice assigned to either treatment or control groups. Italicized numbers above each bar represent pre-treatment tumor volumes (mm^3) of mice. (D) Survival data demonstrating a statistically significant survival benefit of dasatinib *versus* saline vehicle for doses of 95 mg/kg ($P < .001$).

25% or less). Studies are underway to further characterize pharmacokinetic parameters and optimize dose-response *in vivo*.

Net Accumulation of Micellar ^{18}F-SKI249380 in mGBM

Biodistribution and blood, renal, and hepatobiliary clearance were evaluated for i.v. tracer doses of micellar ^{18}F-SKI249380 to glioma-bearing mice, as this formulation resulted in the highest tumor uptake and was well tolerated. Image-derived maximum uptake values in tumor-bearing brain only decreased by about 35% over a 4-hour time period p.i.; an average uptake value of 2.03%ID/g was measured at 4 hours (Figure W4A). High, but progressively decreasing, hepatobiliary activity was found over the imaging period. At 4 hours
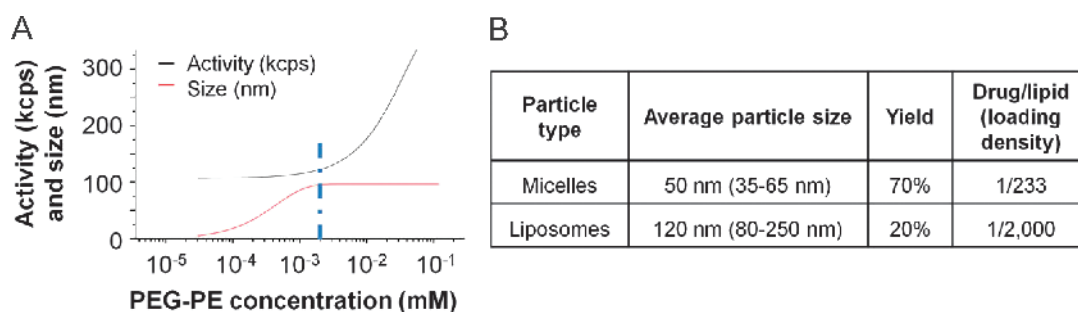
Figure 5. *In vitro* lipid formulations of ^{18}F-SKI249380 for PDGFR targeting and characterization. (A) Fitted curves for micelle nanoformulations of ^{18}F-SKI249380 activity (kcps) and size (nm) as a function of PEG-PE concentration. The CMC (blue line), ^{18}F-SKI249380-to-lipid loading efficiency (1:20 max), and maximum diameter (red line, up to 100 nm) are derived. (B) Nanocarrier size, respective yields, and ^{18}F-SKI249380 loading densities.
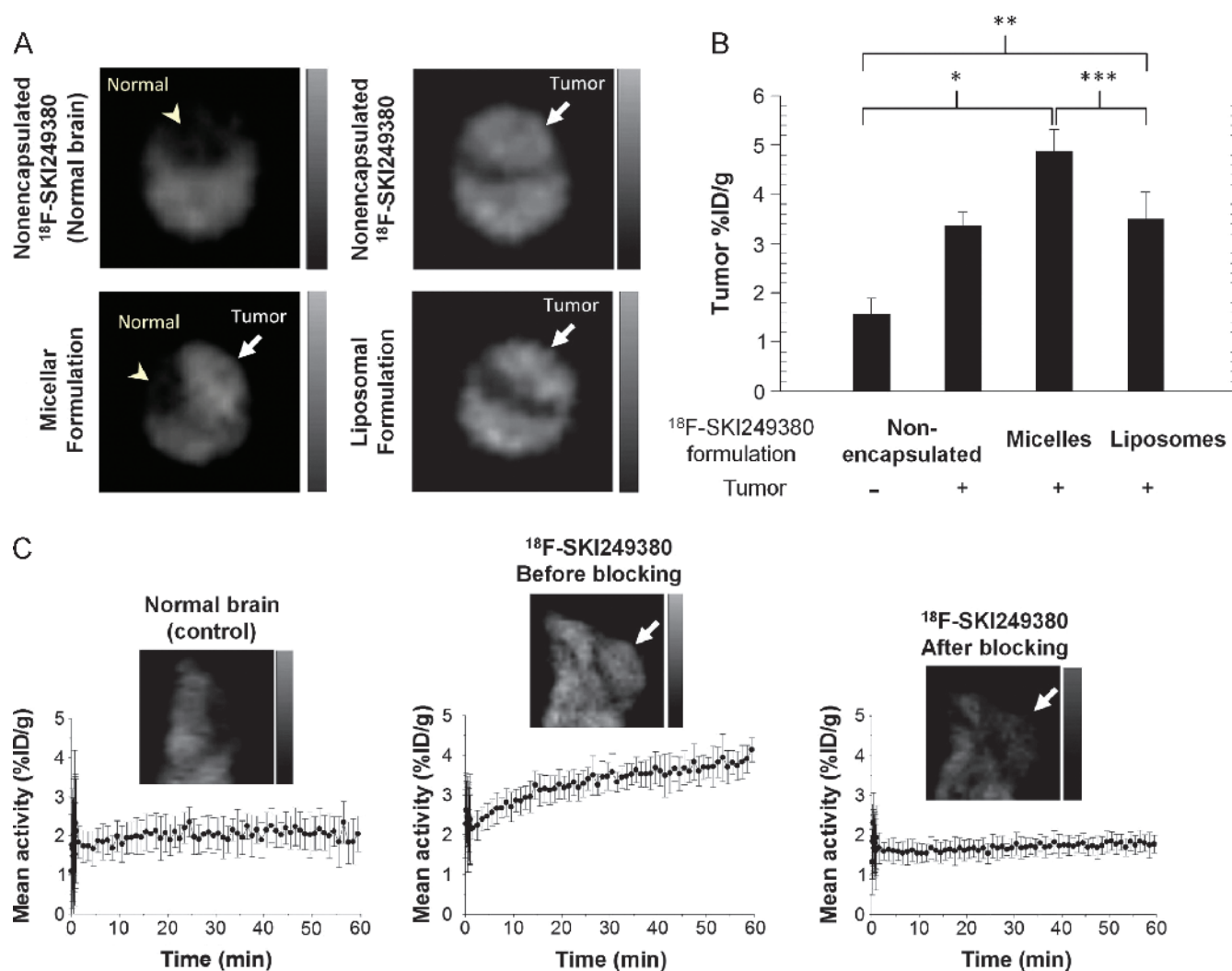
Figure 6. *In vivo* dynamic PET imaging of selective targeting and uptake of unencapsulated and nanoformulated ^{18}F-SKI249380 in mGBM. (A) Representative axial microPET images at 1 hour p.i., demonstrating uptake of unencapsulated ^{18}F-SKI249380 and micelle- or liposome-formulated ^{18}F-SKI249380 in tumor-bearing brains (arrows) as against non–tumor-bearing (control) brain (arrowhead). (B) Graphical summary of tumor uptake values (%ID/g) for treatment and control groups. (C) Representative sagittal microPET brain images from control and tumor-bearing (arrows) animals i.v. injected with ^{18}F-SKI249380, the latter before (pre-block) and after (post-block) blocking with pharmacologic doses of dasatinib. Corresponding 1-hour TACs are shown. Each bar represents mean ± SD. One-tailed Mann-Whitney U tests demonstrated statistical significance at the $P \leq .05$ level for micelles (*$P = .002$) and liposomes (**$P = .014$) relative to controls, as well as between micelles and liposomes (***$P = .016$).

p.i., image-derived uptake values over the liver region (~1.5%ID/g) were found to correspond with uptake values for *ex vivo* gamma-counted specimens (~2.5%ID/g). High uptake values were measured in harvested intestine, spleen, and bone (Figure W4*B*). Blood data are approximated by ROI measurements over the heart. Image-derived renal uptake values were unable to be determined as no evident activity was seen over these regions. At 4 hours p.i., a statistically significant correlation was found between image-derived and *ex vivo* uptake values for liver, heart, tumor-bearing brain, and muscle ($r = 0.98$, $P < .02$; Figure W4*B*, inset).

Discussion

Dasatinib is an oral inhibitor of multiple RTKs, including PDGFR and non-receptor membrane-associated Src tyrosine kinase [11,14]. Nearly all human malignant gliomas demonstrate amplification and over-expression of PDGFRα [31,32], resulting from autocrine stimulation of malignant cells [4,5,9,21]. PDGFR activation in GBMs leads to interactions with Src binding domains, in turn, increasing Src activity [6] and promoting proliferation, invasion, and vasculogenesis [33]. Pre-clinical evidence suggests that Src is frequently phosphorylated in GBM cell lines and activated in human GBM [17,34]. Further, downstream signaling through phosphatidylinositol 3-kinase and mitogen-activated protein pathways is operative, promoting tumorigenesis, proliferation, and angiogenesis.

Dasatinib inhibits Src kinase in multiple cancer cell lines, including melanoma and glioma xenograft models [8,35,36]. In this study, we show that a newly modified fluorinated dasatinib derivative does not alter *in vitro* receptor binding kinetics, specificity, or inhibitory activity in PDGFB-driven primary mGBM cells, relative to dasatinib. ^{19}F-SKI249380 and dasatinib were found to similarly modulate biologic activity over a range of concentrations and time intervals, which resulted in comparable IC$_{50}$ values in the low nanomolar range, equivalent to

those seen with other cell lines [16]. Progressive viability losses, observed with increasing ^{19}F-SKI249380 concentrations to serum-supplemented cells, were found to be higher with PDGF-supplemented media.

Although previously tested in glioma cell lines and xenografts [7,8], dasatinib inhibition of RTKs, non-RTKs, and other phosphorylated pathway intermediates have not been investigated in primary tumor cells harvested from PDGFB-driven mGBM. In NIH 3T3 fibroblast cells, encoding PDGFRα-myc receptors, we showed that ^{19}F-SKI249380 inhibited receptor activity. ^{19}F-SKI249380 inhibited tyrosine kinase activity and phosphorylation of PDGFRα and reduced downstream activation and phosphorylation of MAPK, PI3K, and Src kinase signaling at higher concentrations (150 nM). Inhibition of receptor activity has not been investigated in prior studies. Our results are consistent with those of previous studies using glioma cell lines [7,8], showing reductions in levels of key pathway intermediates (i.e., pSrc, pAkt), after 100 to 250 nM dasatinib. Specifically, we observed a pronounced and sustained inhibition of pSrc kinase (>72 hours), as compared with shorter-lived inhibition of other phosphorylated intermediates of MAPK and PI3K pathways.

Cell cycle studies suggested that ^{19}F-SKI249380 inhibited proliferation in primary glioma cells resulting from G_1 arrest, with clear reductions in the %S phase cells at higher ^{19}F-SKI249380 concentrations. Apoptosis occurred to a lesser degree over the concentration range tested. These mechanisms of action have not been consistently observed for other tumor cell lines incubated with dasatinib. In one prior study [8], glioma cell lines treated with dasatinib demonstrated minimal G_1 arrest, negligible increase in the S phase population, increases in autophagic cell death, and an absence of apoptosis. These effects were also observed for human ovarian cancer [37]. Dasatinib has also been shown to induce apoptosis at nanomolar concentrations in osteosarcomas [33]. Conversely, Johnson et al. [38] revealed dasatinib-induced G_1 phase arrest and apoptotic effects in non–small cell lung cancer and head and neck squamous cell carcinoma.

The ability to flexibly adapt the formulation of clinically promising drugs to improve their physicochemical and/or biologic properties, coupled with metabolic imaging tools for sensitively quantifying preclinical/clinical trial end points, will be crucial to the success of molecular medicine. At present, prescribed drug dosing regimens for treating tumors are based on patient body surface area or weight considerations rather than on the metabolic/functional characteristics of the individual tumor, as established by quantitative imaging approaches. A suitable tracer formulation should exhibit optimum solubility properties under physiologic conditions [39], demonstrate no adverse biologic effects, and facilitate drug transport, delivery [40], and tumor localization. Improvements in drug solubility may reduce peak concentrations of the drug in the circulation, leading to more favorable pharmacokinetic and metabolic profiles. Blood circulation times may be extended, enhancing bioavailability and localization of pharmaceutical activity to the target tissue. Reductions in the required drug dosage might then be realized, thus minimizing risks of systemic toxicity while increasing treatment efficacy.

In this study, utilization of micellar and liposomal nanocarriers met these requirements. Additionally, the calculated CMC for our micellar preparations suggested that ^{18}F-SKI249380, although initially contained within micelles, should be released from this formulation, largely existing in a free form during the course of the imaging study. Thus, its uptake and distribution should be representative of that observed for dasatinib. On the basis of the estimates of the whole-body fluid compartment, PEG-PE concentrations in micelles were roughly

10 μM, on the order of the CMC. This property of micelles may explain, along with its relatively smaller average size, the greater tumor uptake/accumulation found with micellar tracer preparations of ^{18}F-SKI249380, compared with liposomal preparations. In addition, the improved drug solubility, delivery, and kinetic behavior, conferred by the use of these micellar ^{18}F-SKI249380 preparations, presumably contributed to these findings.

Acknowledgments

## References

[1] Morris PG and Abrey LE (2010). Novel targeted agents for platelet-derived growth factor receptor and c-KIT in malignant gliomas. *Target Oncol* **5**, 193–200.

[2] Holland EC, Hively WP, DePinho RA, and Varmus HE (1998). A constitutively active epidermal growth factor receptor cooperates with disruption of G_1 cell-cycle arrest pathways to induce glioma-like lesions in mice. *Genes Dev* **12**, 3675–3685.

[3] Holland EC, Hively WP, Gallo V, and Varmus HE (1998). Modeling mutations in the G1 arrest pathway in human gliomas: overexpression of *CDK4* but not loss of *INK4a-ARF* induces hyperploidy in cultured mouse astrocytes. *Genes Dev* **12**, 3644–3649.

[4] Dai C, Celestino JC, Okada Y, Louis DN, Fuller GN, and Holland EC (2001). PDGF autocrine stimulation dedifferentiates cultured astrocytes and induces oligodendrogliomas and oligoastrocytomas from neural progenitors and astrocytes *in vivo*. *Genes Dev* **15**, 1913–1925.

[5] Fomchenko EI and Holland EC (2007). Platelet-derived growth factor-mediated gliomagenesis and brain tumor recruitment. *Neurosurg Clin N Am* **18**, 39–58.

[6] Ahluwalia MS, de Groot J, Liu WM, and Gladson CL (2010). Targeting SRC in glioblastoma tumors and brain metastases: rationale and preclinical studies. *Cancer Lett* **298**, 139–149.

[7] Dumont RA, Hildebrandt I, Su H, Haubner R, Reischl G, Czernin JG, Mischel PS, and Weber WA (2009). Noninvasive imaging of $\alpha_v\beta_3$ function as a predictor of the antimigratory and antiproliferative effects of dasatinib. *Cancer Res* **69**, 3173–3179.

[8] Milano V, Piao Y, LaFortune T, and de Groot J (2009). Dasatinib-induced autophagy is enhanced in combination with temozolomide in glioma. *Mol Cancer Ther* **8**, 394–406.

[9] Sathornsumetee S, Rich JN, and Reardon DA (2007). Diagnosis and treatment of high-grade astrocytoma. *Neurol Clin* **25**, 1111–1139.

[10] Wen PY, Yung WK, Lamborn KR, Dahia PL, Wang Y, Peng B, Abrey LE, Raizer J, Cloughesy TF, Fink K, et al. (2006). Phase I/II study of imatinib mesylate for recurrent malignant gliomas: North American Brain Tumor Consortium Study 99-08. *Clin Cancer Res* **12**, 4899–4907.

[11] Chen Z, Lee FY, Bhalla KN, and Wu J (2006). Potent inhibition of platelet-derived growth factor-induced responses in vascular smooth muscle cells by BMS-354825 (dasatinib). *Mol Pharmacol* **69**, 1527–1533.

[12] Kamath AV, Wang J, Lee FY, and Marathe PH (2008). Preclinical pharmacokinetics and *in vitro* metabolism of dasatinib (BMS-354825): a potent oral multi-targeted kinase inhibitor against SRC and BCR-ABL. *Cancer Chemother Pharmacol* **61**, 365–376.

[13] Luo FR, Yang Z, Camuso A, Smykla R, McGlinchey K, Fager K, Flefleh C, Castaneda S, Inigo I, Kan D, et al. (2006). Dasatinib (BMS-354825) pharmacokinetics and pharmacodynamic biomarkers in animal models predict optimal clinical exposure. *Clin Cancer Res* **12**, 7180–7186.

[14] Shah NP, Tran C, Lee FY, Chen P, Norris D, and Sawyers CL (2004). Overriding imatinib resistance with a novel ABL kinase inhibitor. *Science* **305**, 399–401.

[15] Veach DR, Namavari M, Pillarsetty N, Santos EB, Beresten-Kochetkov T, Lambek C, Punzalan BJ, Antczak C, Smith-Jones PM, Djaballah H, et al. (2007). Synthesis and biological evaluation of a fluorine-18 derivative of dasatinib. *J Med Chem* **50**, 5853–5857.

[16] Pichot CS, Hartig SM, Xia L, Arvanitis C, Monisvais D, Lee FY, Frost JA, and Corey SJ (2009). Dasatinib synergizes with doxorubicin to block growth, migration, and invasion of breast cancer cells. *Br J Cancer* **101**, 38–47.

[17] Du J, Bernasconi P, Clauser KR, Mani DR, Finn SP, Beroukhim R, Burns M, Julian B, Peng XP, Hieronymus H, et al. (2009). Bead-based profiling of tyrosine kinase phosphorylation identifies SRC as a potential target for glioblastoma therapy. *Nat Biotechnol* **27**, 77–83.

[18] Ozawa T, Brennan CW, Wang L, Squatrito M, Sasayama T, Nakada M, Huse JT, Pedraza A, Utsuki S, Yasui Y, et al. (2010). PDGFRA gene rearrangements are frequent genetic events in PDGFRA-amplified glioblastomas. *Genes Dev* **24**, 2205–2218.

[19] Kedar U, Phutane P, Shidhaye S, and Kadam V (2010). Advances in polymeric micelles for drug delivery and tumor targeting. *Nanomedicine* **6**, 714–729.

[20] Holland EC and Varmus HE (1998). Basic fibroblast growth factor induces cell migration and proliferation after glia-specific gene transfer in mice. *Proc Natl Acad Sci USA* **95**, 1218–1223.

[21] Shih AH and Holland EC (2006). Platelet-derived growth factor (PDGF) and glial tumorigenesis. *Cancer Lett* **232**, 139–147.

[22] Bleau AM, Hambardzumyan D, Ozawa T, Fomchenko EI, Huse JT, Brennan CW, and Holland EC (2009). PTEN/PI3K/Akt pathway regulates the side population phenotype and ABCG2 activity in glioma tumor stem-like cells. *Cell Stem Cell* **4**, 226–235.

[23] Hambardzumyan D, Amankulor NM, Helmy KY, Becher OJ, and Holland EC (2009). Modeling adult gliomas using RCAS/t-va technology. *Transl Oncol* **2**, 89–95.

[24] Birdi K (1997). *Handbook of Surface and Colloid Chemistry*. CRC Press, Boca Raton, FL.

[25] Holland EC, Celestino J, Dai C, Schaefer L, Sawaya RE, and Fuller GN (2000). Combined activation of Ras and Akt in neural progenitors induces glioblastoma formation in mice. *Nat Genet* **25**, 55–57.

[26] Hu X, Pandolfi PP, Li Y, Koutcher JA, Rosenblum M, and Holland EC (2005). mTOR promotes survival and astrocytic characteristics induced by Pten/AKT signaling in glioblastoma. *Neoplasia* **7**, 356–368.

[27] Momota H, Nerio E, and Holland EC (2005). Perifosine inhibits multiple signaling pathways in glial progenitors and cooperates with temozolomide to arrest cell proliferation in gliomas *in vivo*. *Cancer Res* **65**, 7429–7435.

[28] Courtneidge SA, Kypta RM, Cooper JA, and Kazlauskas A (1991). Platelet-derived growth factor receptor sequences important for binding of src family tyrosine kinases. *Cell Growth Differ* **2**, 483–486.

[29] Gelderloos JA, Rosenkranz S, Bazenet C, and Kazlauskas A (1998). A role for Src in signal relay by the platelet-derived growth factor α receptor. *J Biol Chem* **273**, 5908–5915.

[30] Kypta RM, Goldberg Y, Ulug ET, and Courtneidge SA (1990). Association between the PDGF receptor and members of the src family of tyrosine kinases. *Cell* **62**, 481–492.

[31] Hermanson M, Funa K, Hartman M, Claesson-Welsh L, Heldin CH, Westermark B, and Nister M (1992). Platelet-derived growth factor and its receptors in human glioma tissue: expression of messenger RNA and protein suggests the presence of autocrine and paracrine loops. *Cancer Res* **52**, 3213–3219.

[32] Nister M, Libermann TA, Betsholtz C, Pettersson M, Claesson-Welsh L, Heldin CH, Schlessinger J, and Westermark B (1988). Expression of messenger RNAs for platelet-derived growth factor and transforming growth factor-alpha and their receptors in human malignant glioma cell lines. *Cancer Res* **48**, 3910–3918.

[33] Shor AC, Keschman EA, Lee FY, Muro-Cacho C, Letson GD, Trent JC, Pledger WJ, and Jove R (2007). Dasatinib inhibits migration and invasion in diverse human sarcoma cell lines and induces apoptosis in bone sarcoma cells dependent on SRC kinase for survival. *Cancer Res* **67**, 2800–2808.

[34] Takenaka N, Mikoshiba K, Takamatsu K, Tsukada Y, Ohtani M, and Toya S (1985). Immunohistochemical detection of the gene product of Rous sarcoma virus in human brain tumors. *Brain Res* **337**, 201–207.

[35] Eustace AJ, Crown J, Clynes M, and O'Donovan N (2008). Preclinical evaluation of dasatinib, a potent Src kinase inhibitor, in melanoma cell lines. *J Transl Med* **6**, 53–63.

[36] Buettner R, Mesa T, Vultur A, Lee F, and Jove R (2008). Inhibition of Src family kinases with dasatinib blocks migration and invasion of human melanoma cells. *Mol Cancer Res* **6**, 1766–1774.

[37] Konecny GE, Glas R, Dering J, Manivong K, Qi J, Finn RS, Yang GR, Hong KL, Ginther C, Winterhoff B, et al. (2009). Activity of the multikinase inhibitor dasatinib against ovarian cancer cells. *Br J Cancer* **101**, 1699–1708.

[38] Johnson FM, Saigal B, Talpaz M, and Donato NJ (2005). Dasatinib (BMS-354825) tyrosine kinase inhibitor suppresses invasion and induces cell cycle arrest and apoptosis of head and neck squamous cell carcinoma and non–small cell lung cancer cells. *Clin Cancer Res* **11**, 6924–6932.

[39] Torchilin VP, Lukyanov AN, Gao Z, and Papahadjopoulos-Sternberg B (2003). Immunomicelles: targeted pharmaceutical carriers for poorly soluble drugs. *Proc Natl Acad Sci USA* **100**, 6039–6044.

[40] Musacchio T and Torchilin VP (2011). Recent developments in lipid-based pharmaceutical nanocarriers. *Front Biosci* **16**, 1388–1412.
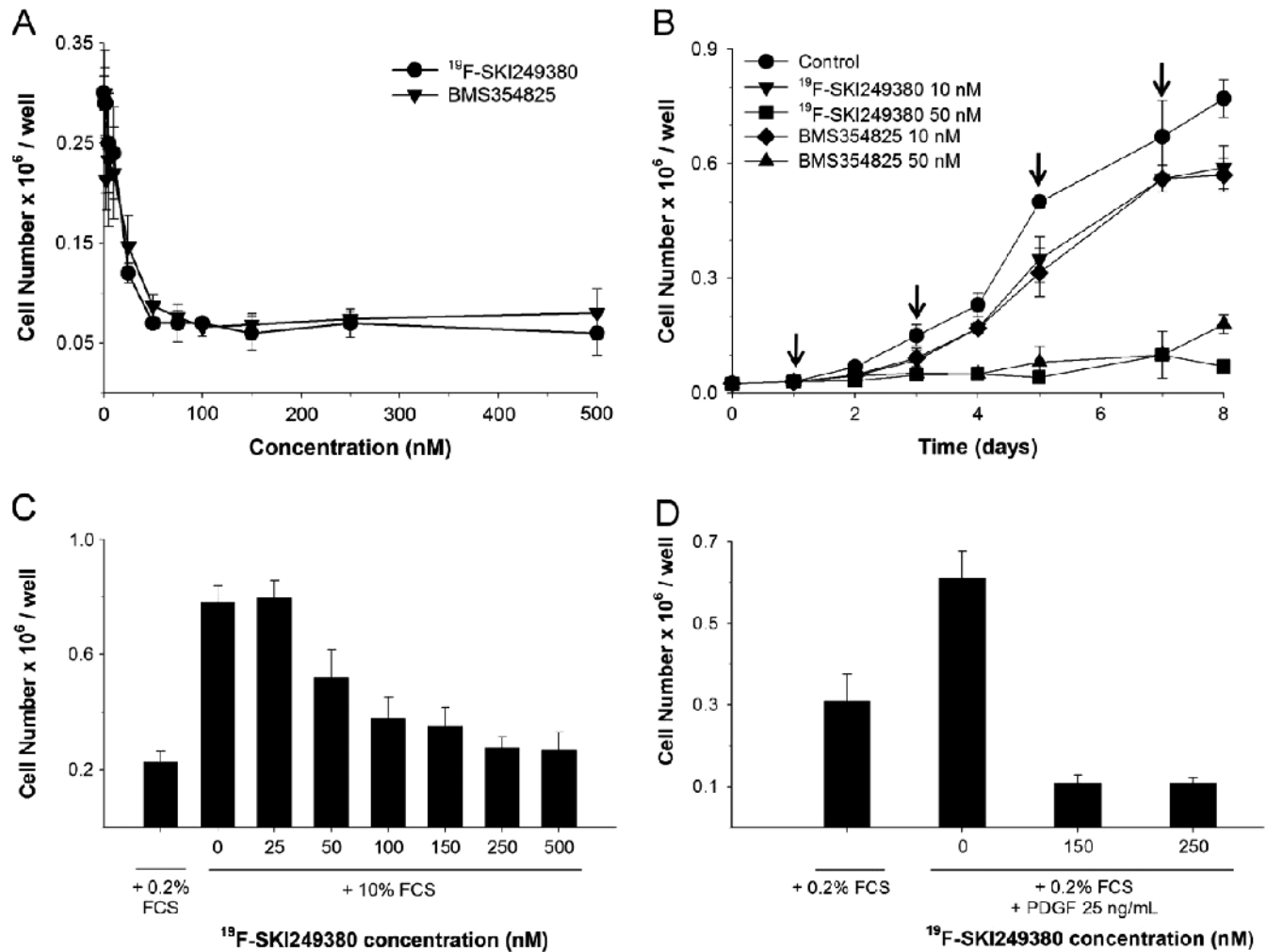
Figure W1. PDGFB-driven mGBM cell survival and proliferation are inhibited by increasing concentrations of ^{19}F-SKI249380 and dasatinib. (A) Cell viability loss as a function of drug concentration in DMEM-HG media supplemented with 10% FCS. (B) Differences in viability and growth rate of mGBM cells incubated with ^{19}F-SKI249380 or dasatinib as a function of time at two different concentrations. (C) ^{19}F-SKI249380 reductions in the viability of mGBM cells initially quiescent (serum-deprived conditions) but subsequently induced by 10% FCS–supplemented media. (D) Same as in C but induced by 0.2% FCS and PDGF-BB supplementation. Control wells contain 0.2% FCS. Experiments performed in triplicate.
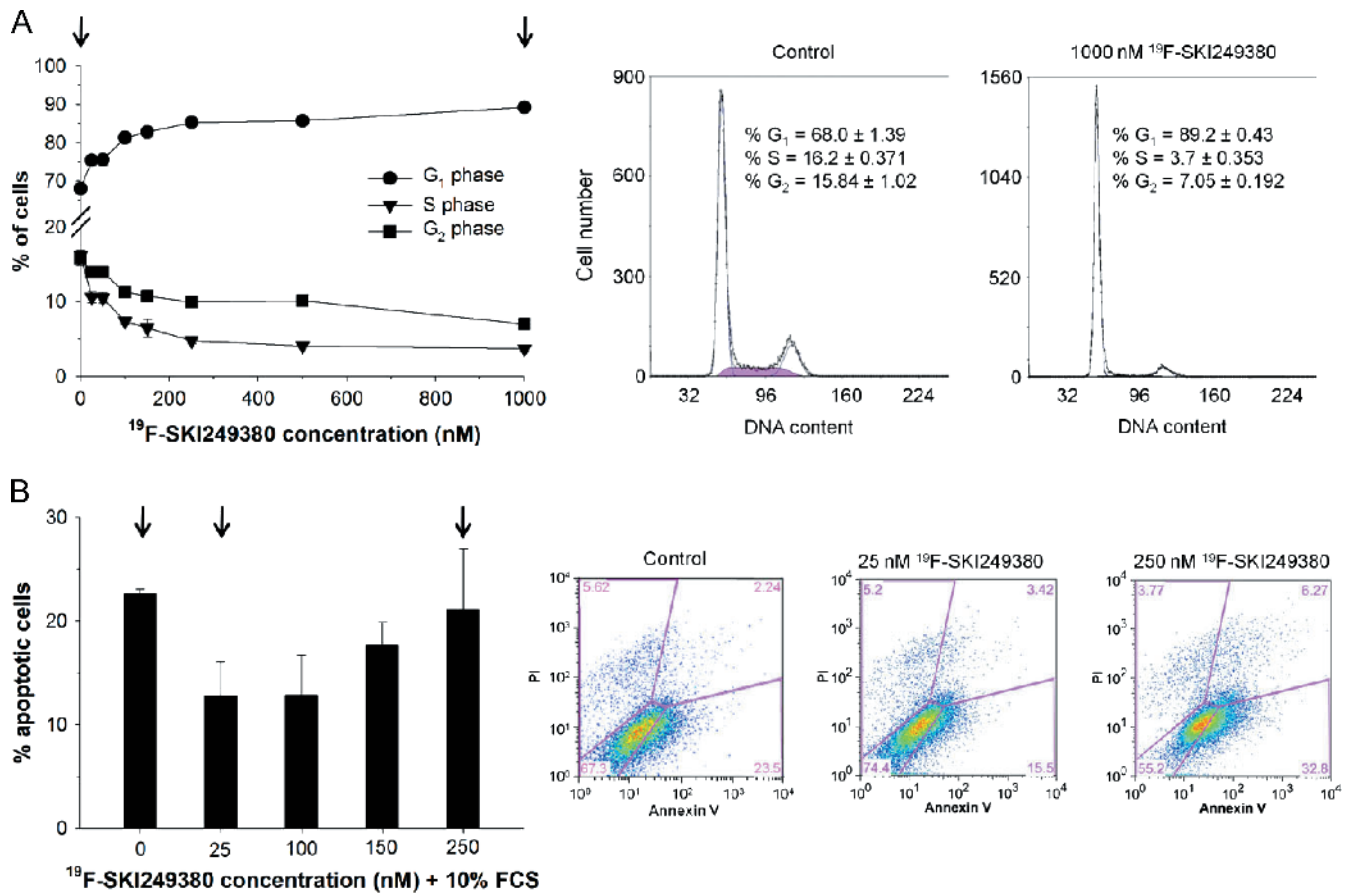
Figure W2. ^{19}F-SKI249380 promotes G_1 arrest, marked reductions in S phase (proliferative phase) activity, and increased apoptosis. (A) Percentage (%) of viable cells in the G_1, S, and G_2 phases of the cell cycle as a function of ^{19}F-SKI249380 concentration. Representative histograms (arrows) are shown for cells under control (i.e., no drug) conditions and after incubation with 1 μM ^{19}F-SKI249380. (B) Percentage of apoptotic cells as a function of ^{19}F-SKI249380 concentration. Representative histograms (arrows) for three drug concentrations indicate percentage of apoptotic cells (lower right-hand corner). Experiments were performed in triplicate.
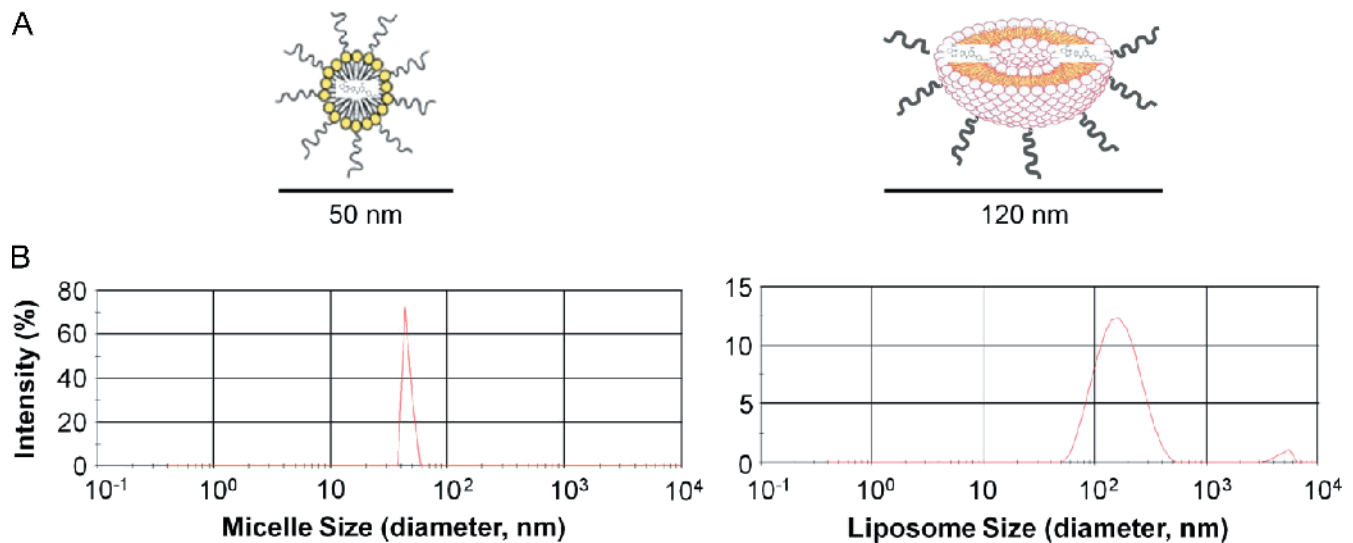
Figure W3. *In vitro* lipid formulations of ^{18}F-SKI249380 for PDGFR targeting and characterization. (A) Schematic of a representative micelle (left) and liposome (right). (B) Micelle (left) and liposome (right) size distribution by intensity.
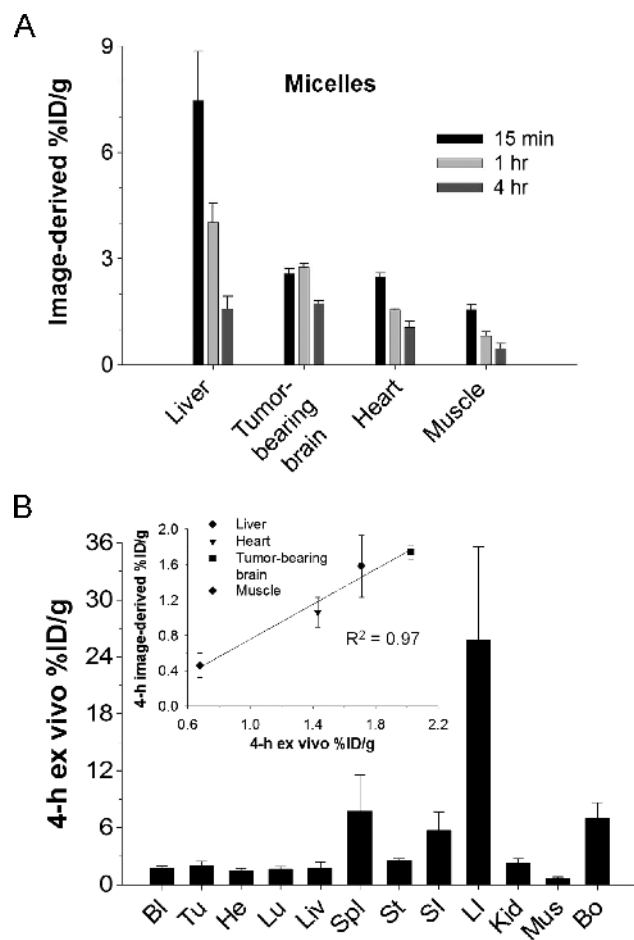
Figure W4. MicroPET image–derived and *ex vivo* γ-counted bio-distribution data following injection of glioma-bearing mice with micelle nanoformulations of ^{18}F-SKI249380. (A) Image-derived mean uptake values for organs/tissues in glioma mice at various times from 15 minutes to 4 hours after i.v. injection of micelle-encapsulated ^{18}F-SKI249380. (B) *Ex vivo* uptake values for γ-counted tissues/organs acquired 4 hours after injection. Inset: Correlation of *in vivo* and *ex vivo* tissue %ID/g values at 4 hours p.i. Each bar represents mean ± SD. Bl, blood; Tu, tumor; He, heart; Lu, lung; Liv, liver; Spl, spleen; St, stomach; SI, small intestine; LI, large intestine; Kid, kidney; Mus, muscle; Bo, bone.